


Article

# Implementation of Three-Dimensional Inverse Design and Its Application to Improve the Compressor Performance

Yu Duan <sup>1,\*</sup>, Qun Zheng <sup>1</sup>, Bin Jiang <sup>1</sup>, Aqiang Lin <sup>2</sup>  and Wenfeng Zhao <sup>1</sup>

<sup>1</sup> College of Power and Energy Engineering, Harbin Engineering University, Harbin 150001, China; zhengqun@hrbeu.edu.cn (Q.Z.); jl725@hrbeu.edu.cn (B.J.); 1244511561@hrbeu.edu.cn (W.Z.)

<sup>2</sup> School of Power and Energy, Northwestern Polytechnical University, Xi'an 710129, China; linaqiang@nwpu.edu.cn

\* Correspondence: duanyu1993@hrbeu.edu.cn

Received: 23 June 2020; Accepted: 12 October 2020; Published: 15 October 2020



**Abstract:** The implementation of a three-dimensional viscous inverse design used for an axial compressor is introduced in this paper. The derivation process of the inverse design algorithm is also described in detail. Moreover, an improved blade update method and a modified relaxation factor are included to enhance the inverse design algorithm. The inverse design is built on an in-house inverse design module coupled with commercial Computational Fluid Dynamic (CFD) software NUMECA™. In contrast to analysis design, the pressure loading and the normal thickness distribution along the blade surfaces are prescribed during the process of inverse design. The numerical methods used to solve the flow field are verified using the experimental data of the transonic fan rotor NASA Rotor 67. A recovery test for the Rotor 67 is carried out to validate the developed three-dimensional inverse design tool. To explore the potential application of the inverse design system, it is then used to improve the aerodynamic performance of a transonic fan Rotor 67 and a multi-row compressor Stage 35 at a near peak efficiency point by reorganizing the pressure loading distribution on the blade surfaces.

**Keywords:** aerodynamic design; compressors; efficiency

## 1. Introduction

In traditional aerodynamic design methods, the blade profile is constructed according to the designed velocity diagrams, selected incidence angles, and deviation angles predicted by empirical equations. The aerodynamic performance of the preliminary blade is then evaluated using the CFD technique. If the flow field predicted by CFD does not meet the design requirements, the preliminary blade profile needs to be manually modified by designers depending on their design experience until the expected flow is realized. This design method is generally referred to as analysis design. It is a repeated and time-consuming process to achieve the design intent because the relationship between the flow and the blade profile is implicit and the design result strongly depends on the accumulation of the designers' experience.

However, this is different for the inverse design, where the blade profile is not prescribed and modified by designers. The blade profile, which corresponds to the prescribed design variables on blade surfaces such as pressure loading or static pressure, is solved as the final solution of the inverse design calculation. In this way, the explicit relationship between the flow field and the blade profile is established in contrast with the analysis design. That means that the inverse design could provide a direct way to control the flow as well as to avoid unguided artificial modifications to blade

shapes. Therefore, the inverse design does not need a repeated process to approximate the target blade. This could facilitate design processes and save computational resources. In inverse design, there are different combinations of design variables. In this paper, the pressure loading and normal thickness distribution along blade surfaces are selected and prescribed as the inverse design variables.

Historically, there were many different inverse design methods. In earlier research, works about inverse design methods were based on the analytical solution of two-dimensional potential flow equations, where the flow was treated as inviscid and irrotational [1,2]. These inverse design methods were rather rough. In fact, there were many limitations in their practical application, because the actual flow in turbomachinery is very complex and not consistent with the hypothesis of potential flow. Moreover, the extension of these methods to three-dimensional flow was not easy to carry out. Nevertheless, those early studies had a certain theoretical significance and ignited further research into inverse design.

With the rapid development of the CFD technique, numerical simulations of three-dimensional viscous flow and even multiphase flow became possible [3,4]. It further helped to understand more details of the internal flow in turbomachinery. Dang, Isgro, Damle, and Qiu and Tiow and Zangeneh developed inverse design methods based on permeable or transpiring models [5–7]. In their inverse design methods, the blade surfaces were regarded to be permeable and flexible where the normal velocity was allowed to exist during the inverse design process. The normal velocity on the blade surfaces was caused by the difference between the local and target pressure loading. These non-tangent flow fields and blade shapes were updated by imposing flow tangency conditions on the blade surfaces. When the inverse design calculation was approaching convergence, the normal velocity on the blade surfaces would disappear and the local pressure loading would tend to the target loading along the blade surfaces. On this basis, Qiu proposed an improved inverse design boundary condition which was shown to be more robust, especially in three-dimensional flows [8]. In Qiu's method, characteristic propagations were added to derive the inverse design algorithm. That is to say, the characteristic variables which propagated in the computational domain were preserved on the upper and lower blade surfaces. This was a significant breakthrough in the research of inverse design. A similar principle was also described in the study of Demeulenaere and Van den Braembussche [9]. In terms of the application of inverse design, some achievements have been made in swept blades, the suppression of secondary flow, multipoint design, blade optimization, and multistage matching [10–13]. However, these inverse design methods have not been widely used. This is because the implementation of these inverse design methods needs to convert the analysis codes to inverse design codes by replacing the wall boundary condition of analysis codes with permeable or transpiring models. Besides this, the blade shape has to be iteratively updated. This would induce a great change in the original program structure. Thus, the obstacle is caused to popularize these inverse design methods especially for the people who do not have analysis codes.

Daneshkhah and Ghaly came up with the concept of virtual velocity based on the work of Thompkins and Tong and proposed an inverse design method which was built on flux conservation [14–16]. This concept of virtual velocity separated the inverse design process into blade deformation and flow analysis. Hence, during the inverse design process, the blade deformation module could be coded individually and the analysis solver could be used without any modification. As a result, the difficulty of implementing inverse design was greatly reduced in this way. It is convenient to select appropriate and remarkable flow solvers including commercial, open-source, or in-house codes according to the actual situation. Similarly, in the work of Van Rooij and Medd, the no-slip condition was included in their original inversed design method to calculate the virtual velocity on the blade surfaces [17]. It was made fully consistent with viscous flow modeling and thus eliminated the difference in boundary conditions between the flow analysis and the inverse design calculation. Another variant of this approach based on virtual velocity could refer to the research of Mileshin, Orekhov, Shchipin, and Startsev [18] and Shumal, Nili-Ahmadabadi, and Shirani [19].

Yang, Liu, Wang, and Wu gave a detailed explanation of the advantages of this inverse design method in comparison with other inverse design approaches [20].

In this paper, we develop an inverse design method which is built on characteristic propagations and the concept of virtual velocity by imposing the no-slip viscous condition. Besides this, a modified blade update algorithm and an improved relaxation factor are included to enhance the inverse design method. The blade smooth technique is also added to guarantee the manufacturability of inverse design blades. In the current study, there are two smooth methods provided to select from. One is NURBS (non-uniform rational B-spline); the other is cubic polynomial. In this paper, the latter is used. The above contents are coded in the in-house inverse design module, which is coupled with commercial CFD software NUMECA™ to accomplish the inverse design.

Rotor 67 is a transonic fan rotor which was designed and tested by the NASA Lewis Research Center. In the public literature [21], the experiment data about the flow field and the performance of Rotor 67 were documented in detail. It is used to verify the numerical methods adopted in this paper. In addition, a recovery test for Rotor 67 is carried out to assess the developed inverse design tool. The test results validate the inverse design methods. Then, two redesign cases are implemented in order to demonstrate the potential application of the inverse design. The transonic fan Rotor 67 and the multi-row compressor Stage 35 are redesigned to improve the efficiency at peak efficiency points using the inverse design tool. The peak efficiencies respectively increase from 89.658% to 89.85% in the redesigned Rotor 67 and from 82.749% to 83.011% in the redesigned Stage 35.

## 2. Numerical Methods and Validation

The Reynolds averaged Navier–Stokes equations are solved to predict the flow field. The conservation form of the transient Navier–Stokes equations in the Cartesian coordinates could be written as:

$$\frac{\partial Q}{\partial t} + \frac{\partial f_c}{\partial x} + \frac{\partial g_c}{\partial y} + \frac{\partial h_c}{\partial z} - \left( \frac{\partial f_v}{\partial x} + \frac{\partial g_v}{\partial y} + \frac{\partial h_v}{\partial z} \right) = S \quad (1)$$

where  $Q$  is the conservative variable;  $f_c$ ,  $g_c$ , and  $h_c$  are the convective flux vectors;  $f_v$ ,  $g_v$ , and  $h_v$  are the viscous flux vectors;  $S$  is the source term.

The analysis solver used in the inverse design is the Fine™/Turbo module of NUMECA™ which adopts the conventional control volume method for space discretization with the second-order upwind total variation diminishing (TVD) scheme. The fourth-order Runge–Kutta method is used for time-marching. The Spalart–Allmaras one-equation turbulence model is taken to predict the Reynolds stress for equation enclosure. In addition, in order to improve the computational efficiency, the local time step and multi-grid techniques are added to accelerate the convergence of the flow analysis. The fluid model is specified as perfect gas which follows the equation of state. At the inlet of the computational domain, the total temperature, total pressure, and direction of upstream flow are defined. The back pressure at the outlet is specified with the radial equilibrium equation in the turbomachinery. A single-flow passage simulation with a periodic boundary condition on the lateral faces is implemented to avoid a lot of computational time and resource spending on full passages. The shroud, hub, and blade surfaces are regarded as adiabatic walls with a viscous no-slip boundary condition.

The NASA Rotor 67, which is the first stage rotor of a two-stage fan, is a low-aspect-ratio design transonic rotor with 22 blades. It was designed and tested as a test case by the NASA Lewis Research Center for meeting the need for detailed experimental data of turbomachinery to validate computational methods. The rotor design pressure ratio is 1.63 at a mass flow of 33.25 kg/s with a rotational speed of 16,043 rpm, which causes a tip speed of 429 m/s and an inlet tip relative Mach number of 1.38. The measurement for the rotor overall performance is based on the aerodynamic survey acquired at stations 1 and 2, which are upstream and downstream of the rotor, respectively. The meridional view of the measurement stations is shown in Figure 1. More details about the blade, flow path geometry, and flow field data could be found in the open literature [21].

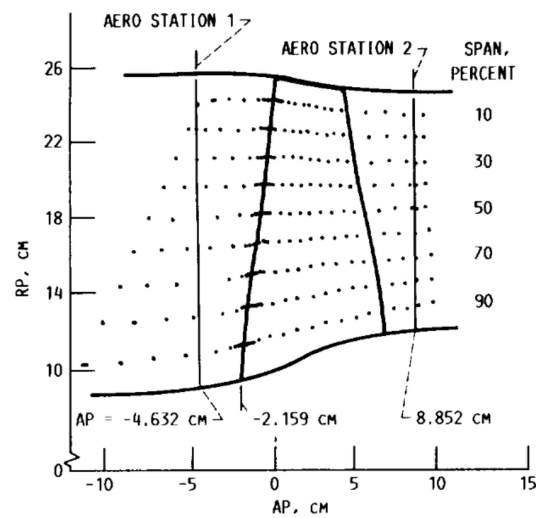


**Figure 1.** Meridional view of the measurement stations (Figure 5. in [21]).

The numerical methods used in this paper are validated by comparing the predicted rotor performance and the flow field with the experimental data. The Rotor 67 model is constructed with 14 blade sections from the hub to shroud and is displayed in Figure 2. The mesh of the computational domain consists of hexahedral elements which are generated using the mesh software AutoGrid5<sup>TM</sup>.

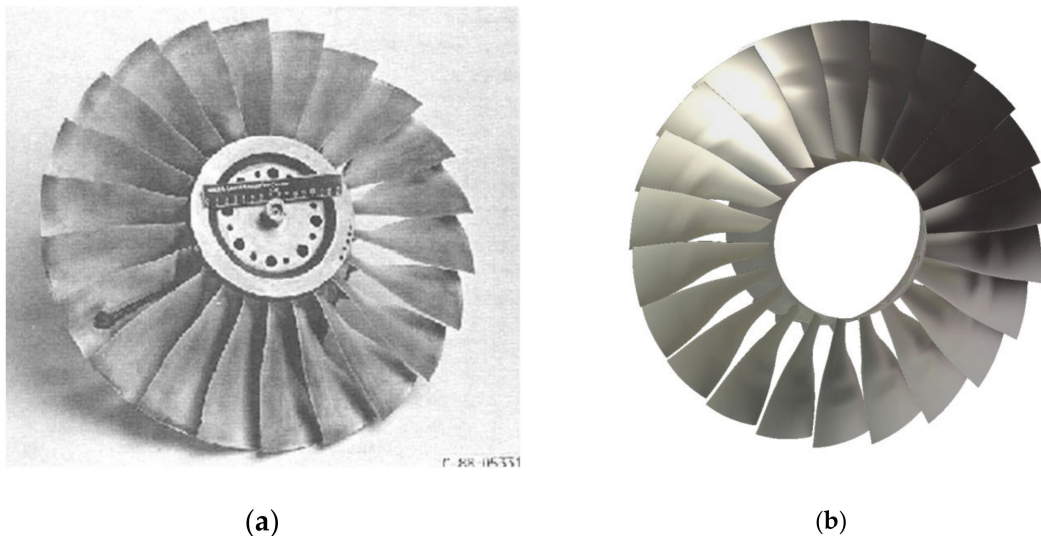


**Figure 2.** Physical model and computational model of Rotor 67: (a) physical model, (b) computational model.

Figure 3 shows the mesh of flow passages in the rotor. As Figure 3 displays, the O4H mesh topology was adopted to split the computational domain. Besides this, the butterfly mesh was used for the tip clearance region. To eliminate the interference of grid number in the numerical simulation, a grid independency test was carried out. Figure 4 shows the predicted mass flow, efficiency, and pressure ratio with  $5 \times 10^5$ ,  $7 \times 10^5$ ,  $10 \times 10^5$ , and  $12 \times 10^5$  grids. This grid independency test demonstrates that finer meshes could hardly improve the simulation in a single flow passage when the grid number is greater than one million. Thus, the grid number of all cases in this paper is specified as one million with 249 axial, 65 tangential, and 61 radial nodes. In addition, 17 radial grids fill the tip clearance considering the tip-leakage flow. The region approaching the shroud, hub, and blade surfaces is carefully refined to resolve the boundary layer and meet the requirement for the  $y$  plus value demanded by the Spalart–Allmaras turbulence model. The  $y$  plus distribution near the blade surfaces is plotted in Figure 5. It shows that the  $y$  plus near the blade surfaces is less than 3.

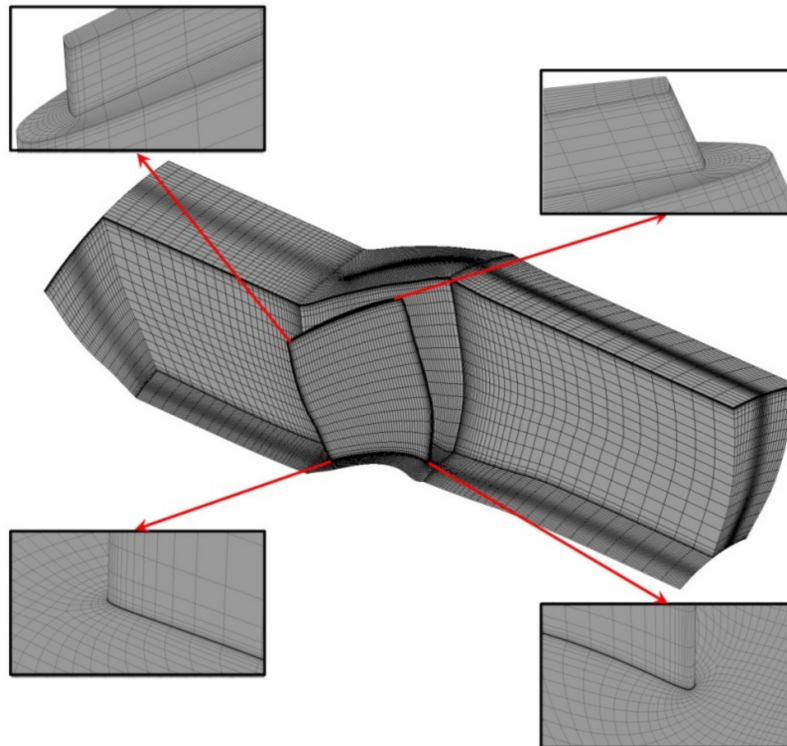
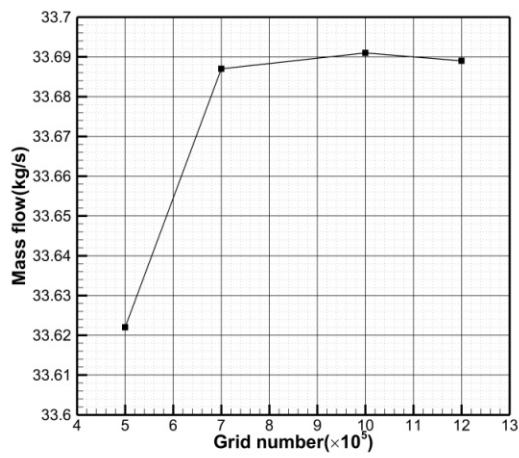
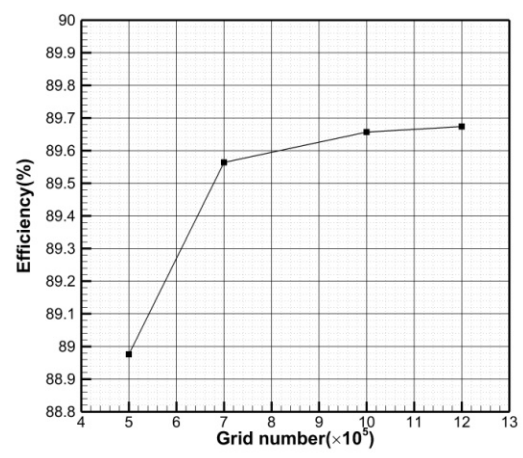


Figure 3. The mesh of the computational domain.



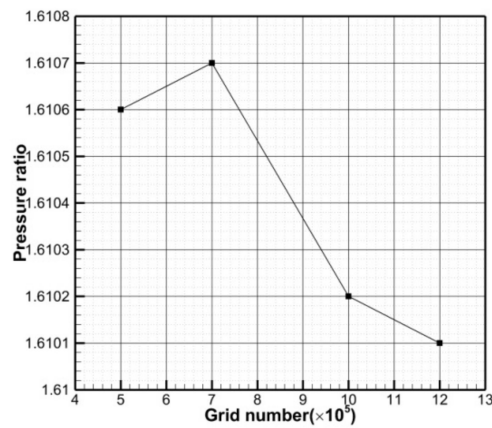
(a)



(b)

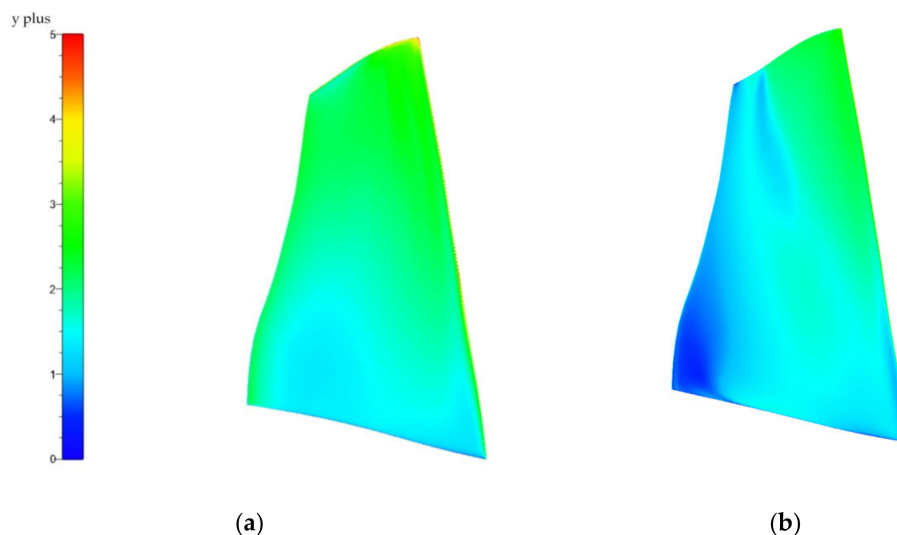
Figure 4. Cont.





(c)

**Figure 4.** Grid independency test: (a) mass flow, (b) efficiency, (c) pressure ratio.



(a)

(b)

**Figure 5.** The y plus near the blade surfaces: (a) y plus near the pressure surface, (b) y plus near the suction surface.

In the process of validating the numerical methods, the predicted pressure ratio and efficiency characteristics are obtained by preserving the total temperature, total pressure, and upstream direction at the inlet and simultaneously adjusting the back pressure at the outlet. Furthermore, the numerical instability point is considered as the near-stall point. Figure 6 displays a comparison of the numerical results with the experimental data using the SA,  $k-\epsilon$ , and SST turbulence models. It demonstrates that the predicted efficiencies and pressure ratios with these three turbulence models are close. Due to the low computational expense of the SA model, it tends to choose the SA one-equation turbulence model. It is found that the efficiency, pressure ratio, and choke mass flow in the simulation are underestimated in comparison with the experimental data. The predicted choke mass flow is 34.6 kg/s, which is 1.03% lower than the measured value of 34.96 kg/s. The predicted total pressure ratio value of 1.66 and the measured pressure ratio value of 1.73, respectively, correspond to 92.77% (32.1 kg/s) of the calculated choke mass flow and 93% (32.51 kg/s) of the measured choke mass flow at the near-stall point. At the near peak efficiency point, the predicted efficiency value is 0.89658, while the measured efficiency is 0.93. These discrepancies between the numerical results and the experiment data are supposed to be mainly caused by the following reasons. The shock wave in the rotor passage has a primary effect on the flow field. However, it is challengeable to accurately predict and capture

the shock wave in the numerical simulations due to the complicated shock structure. Besides this, some complex flow phenomena such as the shockwave/boundary-layer interaction and the tip clearance flow in the transonic flow would adversely affect the accuracy of the numerical simulation. A similar underestimation of the aerodynamic performance of Rotor 67 using fine/turbo was also reported in the work of Zheng et al. [22].

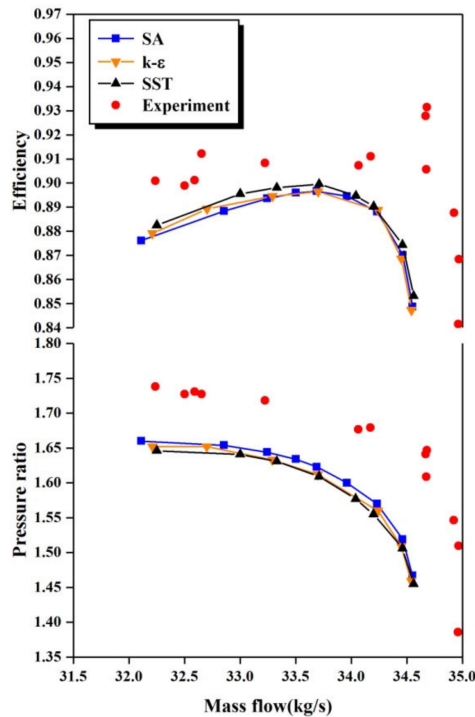


**Figure 6.** The comparison of the numerical results and experimental data.

Figure 7 plots the contour of the relative Mach number under near peak efficiency conditions at the section of 30%, 70%, and 90% spans from the hub. Although there are some discrepancies in predicting the pressure ratio and efficiency characteristics, it is concluded from Figure 7 that the predicted flow field is highly similar to the experimental results. Furthermore, the application of the commercial CFD software NUMECA<sup>TM</sup> to predict the flow field of Rotor 67 with the Spalart–Allmaras turbulence model has been widely validated by many researchers [23–25]. Thus, the predicted results can be considered acceptable for the purposes of this paper.

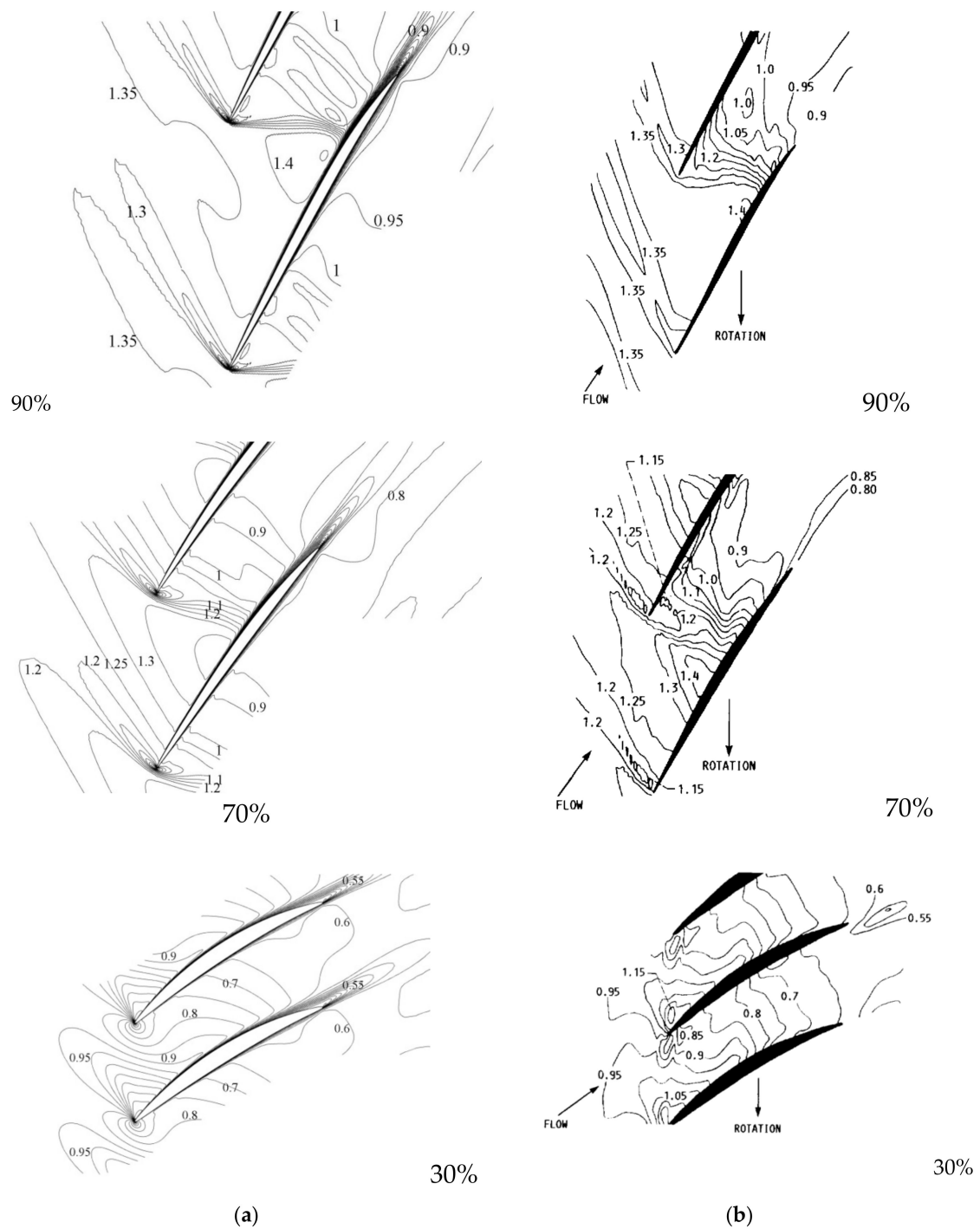


**Figure 7.** The comparison of the simulation and experiment for the flow fields: (a) simulated flow fields at 90%, 70%, and 30% spans from the hub; (b) measured flow fields at 90%, 70%, and 30% spans from the hub.

### 3. Establishment of Inverse Design System

#### 3.1. Inverse Design Method

There are different formulations of inverse design according to the selection of the inverse design variables. Here, the pressure loadings and normal thickness distributions are prescribed as inverse design variables to inquire about the blade mean line.



In order to calculate the virtual velocity on the blade mean line, the wave-propagating characteristics are considered for overcoming the inconsistency caused by the enforcement of the prescribed pressure loading. As shown in Figure 8, the blade surfaces are regarded as flexible and treated as inlet and outlet boundaries in the inverse design method. With the compatibility relations, there are four propagating waves which carry the characteristic variables. The propagation velocities in the direction normal to the blade surfaces are  $W_n$ ,  $W_n$ ,  $W_{n-c}$ , and  $W_{n+c}$ , respectively. Here,  $W_n$  is the normal component of local velocity on the blade surface mesh and  $c$  is the local sound speed in the flow field. The characteristic variables along the four propagating waves are  $\rho + \int \frac{dp}{c^2}$ ,  $W_t$ ,  $W_n - \int \frac{dp}{\rho c}$ , and  $W_n + \int \frac{dp}{\rho c}$ . It is assumed that the characteristic variables which propagate from the interior of the computational domain are preserved when enforcing the target pressure loading and the value of  $W_{n-c}$  is less than zero. Therefore,  $W_n - \int \frac{dp}{\rho c}$  is preserved on the lower surface and  $W_n + \int \frac{dp}{\rho c}$  is preserved on the upper surface. There are approximation relations on the lower and upper surfaces.

$$\rho_{-c-}(W_{n-}^{new} - W_{n-}) - (p_-^{new} - p_-) = 0 \quad (2)$$

$$\rho_{+c+}(W_{n+}^{new} - W_{n+}) + (p_+^{new} - p_+) = 0 \quad (3)$$

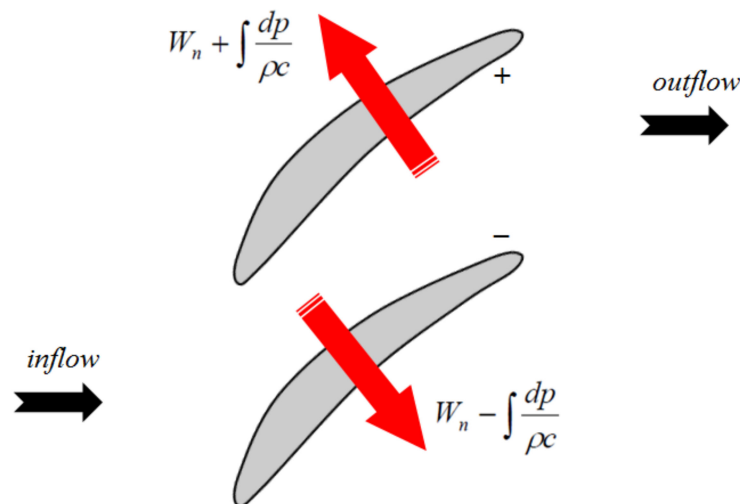


**Figure 8.** The schematic diagram of the inverse design boundary condition.

Subscripts “+” and “-” denote the upper and lower surfaces. Further, the virtual velocity on the blade surfaces could be obtained considering the no-slip condition. The normal velocity on the upper and lower surfaces, respectively, are:

$$W_{n+}^{new} = \frac{p_+ - p_+^{new}}{\rho_{+c+}}, \quad (4)$$

$$W_{n-}^{new} = \frac{p_-^{new} - p_-}{\rho_{-c-}}. \quad (5)$$

Here, the no-slip boundary condition is applied on the blade surfaces so as to be fully consistent with the viscous flow modeling used in flow analysis. This is analogous to the method described by van Rooij and Medd [15].

The static pressure on the upper and lower surfaces is updated using:

$$p_+ = \frac{1}{2}(p_+^{new} + p_-^{new}) + \frac{1}{2}\Delta p \quad (6)$$

$$p_- = \frac{1}{2}(p_+^{new} + p_-^{new}) - \frac{1}{2}\Delta p \quad (7)$$

$\Delta p$  is the prescribed pressure loading. The blade update is realized by the change in the mean line. The corresponding virtual velocity of the mean line is calculated using the average of the virtual velocity on the upper and lower surfaces. The expression of virtual velocity in the mean line could be written by substituting Equations (6) and (7) into Equations (4) and (5).

$$W_v = \frac{1}{2}(W_{n-}^{new} + W_{n+}^{new}) = \frac{(p_-^{new} - p_+^{new}) + \Delta p}{4} \left( \frac{1}{\rho_- c_-} + \frac{1}{\rho_+ c_+} \right) \quad (8)$$

The final displacement of the mean line is calculated using:

$$\Delta d = \Delta t \cdot W_v \quad (9)$$

In previous studies, a constant relaxation factor is used to adjust the inverse time step to control the size of blade displacement. However, the value of the relaxation factor is highly case-dependent. Inspired by the work of Yang et al. [18], the inverse time step is defined as below:

$$\Delta t = \min\left(\frac{0.1\theta}{W_{max}}, 0.02\right) \quad (10)$$

where  $\theta$  is the max normal thickness of the blade and  $W_{max}$  is the largest virtual velocity on the mean line.

In most studies, only the tangential deformation is taken into consideration for simplifying problems when updating the blade. However, some geometrical characteristics may be ignored in this way. A new update method is given here to make a compromise between the precise displacement and the complexity of the blade update.

Figure 9 is depicted to demonstrate the new update method. First, the position of  $i_{ref}$  is figured out according to the virtual velocity at the point  $i$ . Then, the updated position of  $i$  is denoted as  $i_{new}$ . It is the intersection of the straight line  $i_{ref} \sim i-1$  and the axial position of  $i$ .

$$x_{i_{new}} = x_i \quad (11)$$

$$y_{i_{new}} = y_{i-1} + \frac{y_{i_{ref}} - y_{i-1}}{x_{i_{ref}} - x_{i-1}}(x_{i_{new}} - x_{i-1}) \quad (12)$$

The blade smoothing is necessary because geometry oscillations may exist to cause computational instability in the inverse design. This instability is adverse to the convergence of the inverse calculation and even leads to the failure of the inverse design. In addition, from the viewpoint of manufacturing, blade smoothing is beneficial to the mechanical integrity of inverse design blades in practical production. There are two fitting methods provided in the inverse design module to guarantee the smoothing of inverse design blades. The first is called non-uniform rational B-spline (NURBS). This method could approximate a series of discrete points using prescribed control points with minimum error in the least-squares sense. The second is a cubic polynomial, which is also used to connect discrete points smoothly. In all cases in this paper, the cubic polynomial is selected as the fitting method.

It is necessary to note that the inverse design does not run at the whole blade surfaces. In the current method, the inverse design executes from 2–5% to 95–98% of the axial chord. The remaining parts run in analysis mode. This treatment aims to avoid flow complexity near the leading edge and trailing edge.

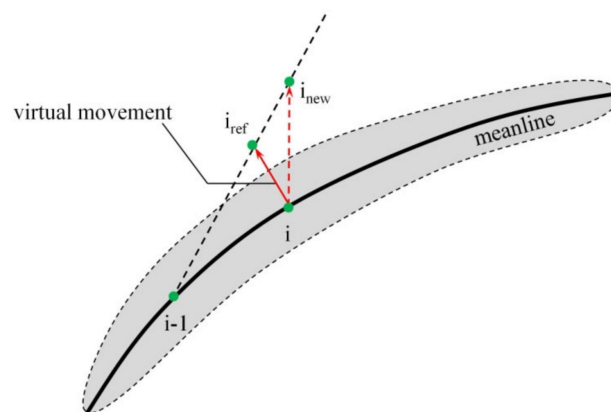


Figure 9. The schematic diagram of the blade update method.

### 3.2. Inverse Design Implementation

Figure 10 shows the process of implementing the inverse design used in this paper. The inverse design system consists of two main modules, which are the in-house inverse design module and the commercial CFD software NUMECA™. The data communication and automatic execution of different modules are realized by batch commands.

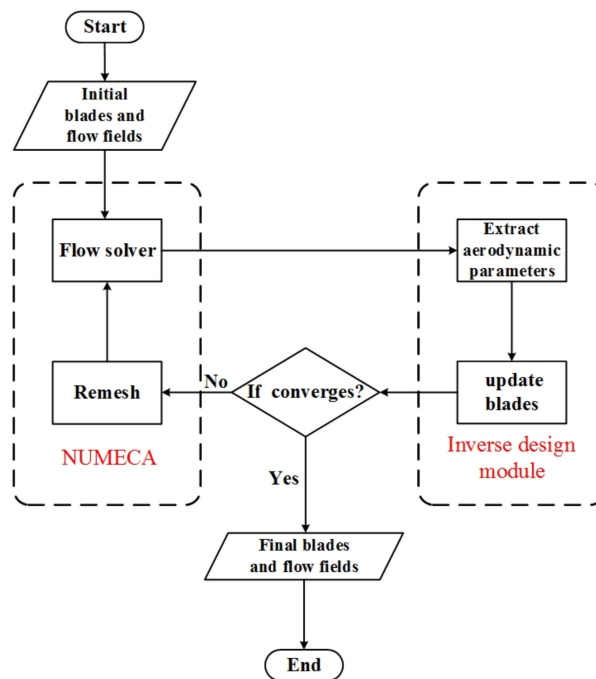


Figure 10. The process of the inverse design system.

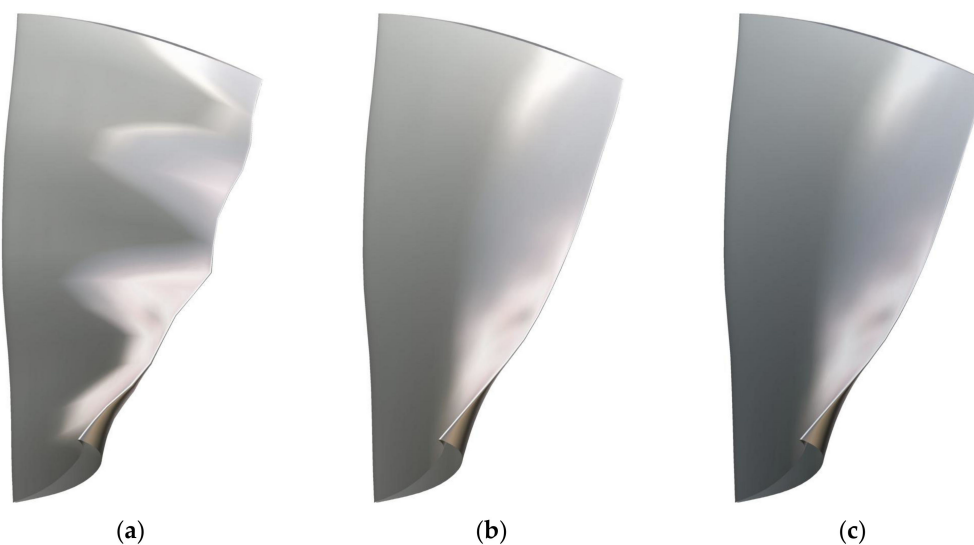
First of all, the initial blade and its corresponding flow field are imported in the flow solver as the initial condition. Then, the aerodynamic and thermodynamic parameters of the flow field are extracted and exported. The induced virtual velocity and displacement of the mean line are determined with the difference in the current pressure loading and the target pressure loading. Next, a new blade is generated using the updated mean line with the given normal thickness distribution. After this, the mesh of the new computational domain is regenerated. The mesh topology and the number of grids are kept the same whenever the mesh is regenerated. Finally, the new mesh is exported to the flow solver and the flow field get updated. The whole inverse design process is repeated until the difference in the current pressure loading with the target pressure loading is under an acceptable tolerance.

### 3.3. Recovery Test

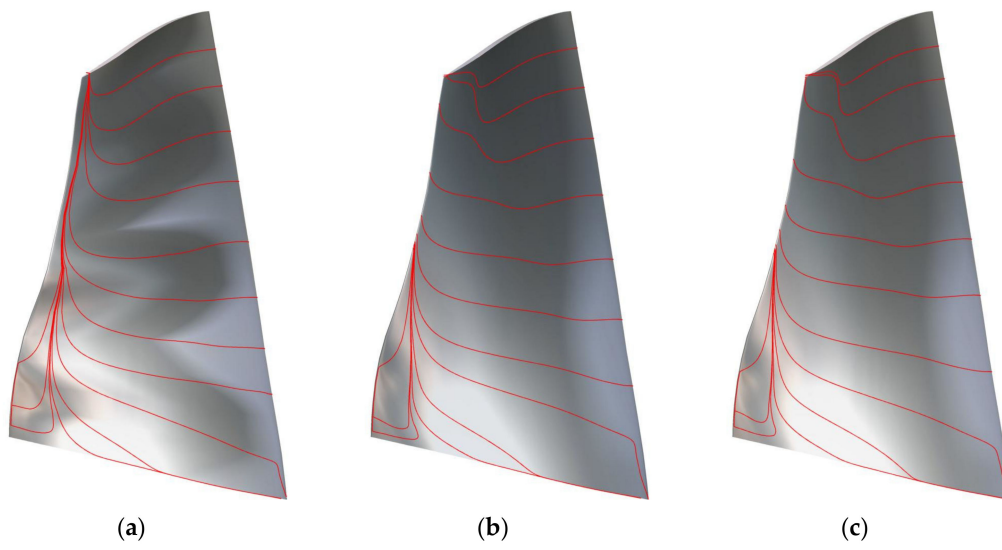
To verify the developed inverse design system, a recovery test for the NASA Rotor 67 is designed and carried out. In the recovery test, the three-dimensional blade is divided into a series of B2B sections along the span of the rotor. Then, the original Rotor 67 is intentionally deformed by changing the blade profiles at 20%, 50%, and 80% spans from the hub as the initial blade in the inverse design. The deformed Rotor 67 shows an irregular and uneven three-dimensional blade surface, as displayed in Figure 11a. The pressure loading of the original Rotor 67 is extracted from the analysis solver and prescribed as the target loading in the recovery test. The normal thickness distribution is also extracted from the original Rotor 67 and kept unchanged in the recovery test. If the initial blade and its flow field could go back to the original when the inverse design is completed, it could be proved that the inverse design system is successful and feasible.

Figure 11b,c plots the shapes of the inverse design and original blades, respectively. The limiting streamlines on the suction surfaces of different blades are depicted in Figure 12a–c. It is observed that there is an increased intensity of the radial flow in the initial blade. Hence, some difference exists in the flow field of the initial blade compared with the original Rotor 67.

From what has been revealed in Figures 11 and 12, this inverse design tool is proved to be successful. The blade geometry, which is the result of inverse design calculation, shows a high similarity with the original Rotor 67. Furthermore, the pattern of the limited streamlines also returns to the original pattern. Figure 13 gives a detailed description of the blade profiles as well as the pressure loadings on blade surfaces at 20%, 50%, and 80% spans from the hub.



**Figure 11.** The comparison of blade shapes: (a) initial blade, (b) inverse design blade, (c) original blade.



**Figure 12.** The limiting streamlines on suction surfaces: (a) initial blade, (b) inverse design blade, (c) original blade.

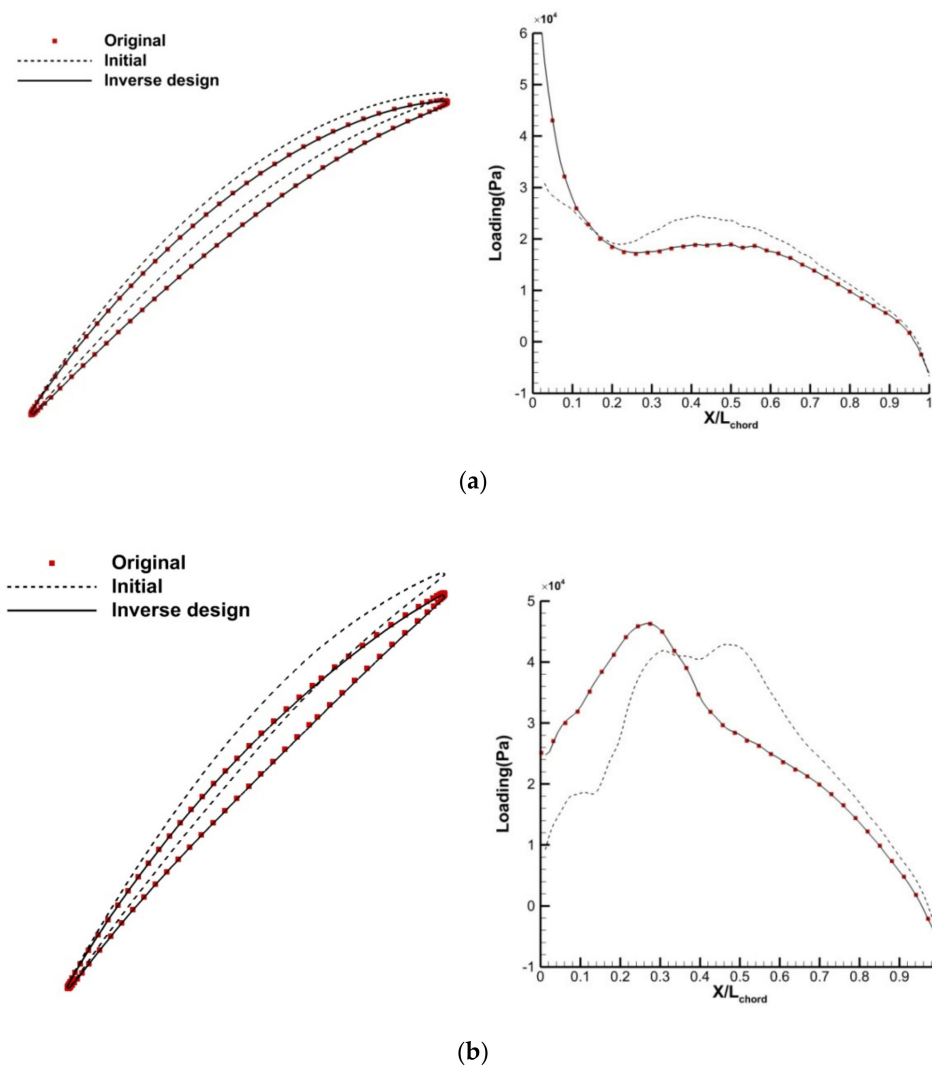


**Figure 13.** Cont.

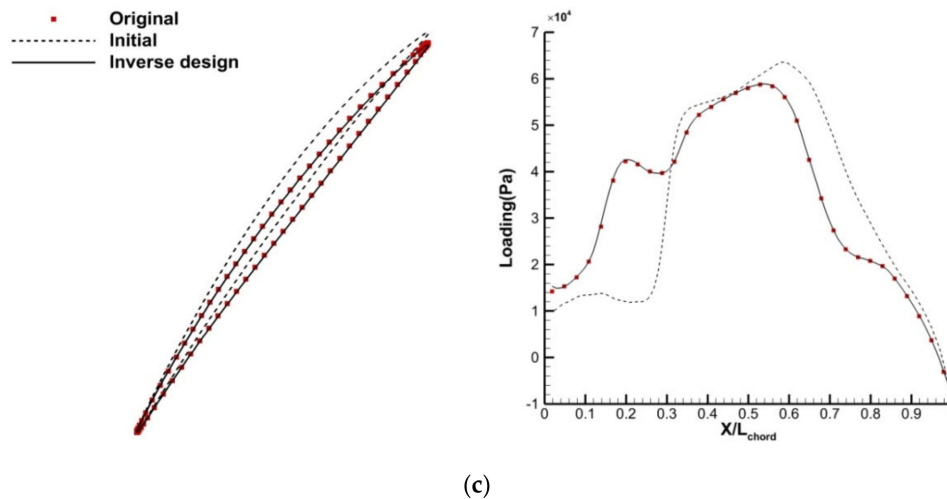


**Figure 13.** Blade profiles and pressure loading distribution in the recovery test: (a) the blade profile and pressure loading at a 20% span, (b) the blade profile and pressure loading at a 50% span, (c) the blade profile and pressure loading at an 80% span.

The success of the recovery test makes great sense. It demonstrates that the inverse design method could force a preliminary blade to the new blade which corresponds the prescribed pressure loading distribution on blade surfaces. The exact recovery of the initial blade to original Rotor 67 proves that the internal process of the inverse design system runs as expected. The excellent reproduction of the target flow field, as shown by the limited streamlines and pressure loading distribution in Figures 12 and 13, indicates that the boundary condition of the inverse design is consistent with the counterpart in the analysis solver when the inverse design calculation converges. To sum up, the consistency in blade shapes and flow fields proves the legitimacy of the inverse design method.

#### 4. The Application of the Inverse Design

##### 4.1. Rotor 67 Redesign

In the first case, the three-dimensional inverse design system is applied to redesign Rotor 67 for improving the efficiency at the near peak efficiency point by reorganizing the pressure loading distribution on the blade surfaces. Before the start of the redesign, an analysis of the flow field of Rotor 67 is made to look for existing problems. It is found that the flow along the span of the rotor could be distinguished as two flow regimes. From the hub to the 40% span, the flow is subsonic. However, the flow is transonic from the 50% span to the blade tip.

The red lines in Figure 14a display the pressure loading distribution of original Rotor 67. In the subsonic flow region, the pressure loading at the leading edge and the induced attack angle are fairly high. What is more, the pressure loading locates more in the rear of the blade. Therefore, it is needed to lower the pressure loading at the leading edge and transfer some pressure loading from the rear to the front for balancing the pressure loading on the blade surfaces. In the transonic flow region, the shock loss is the main loss resource. The peak pressure loading on the blade surfaces represents the strength of the shock wave. Thus, the main effort in the redesign is to reduce the peak pressure loading at the transonic regime. Simultaneously, we attempt to keep the total pressure loading unchanged. Numerical experiments have been implemented, and their results indicated that the redesign from the 80% span to the blade tip could hardly improve the efficiency due to the interaction of the tip clearance flow and the main flow. Therefore, the blade sections from the 80% span to the blade tip are performed in the analysis calculation.



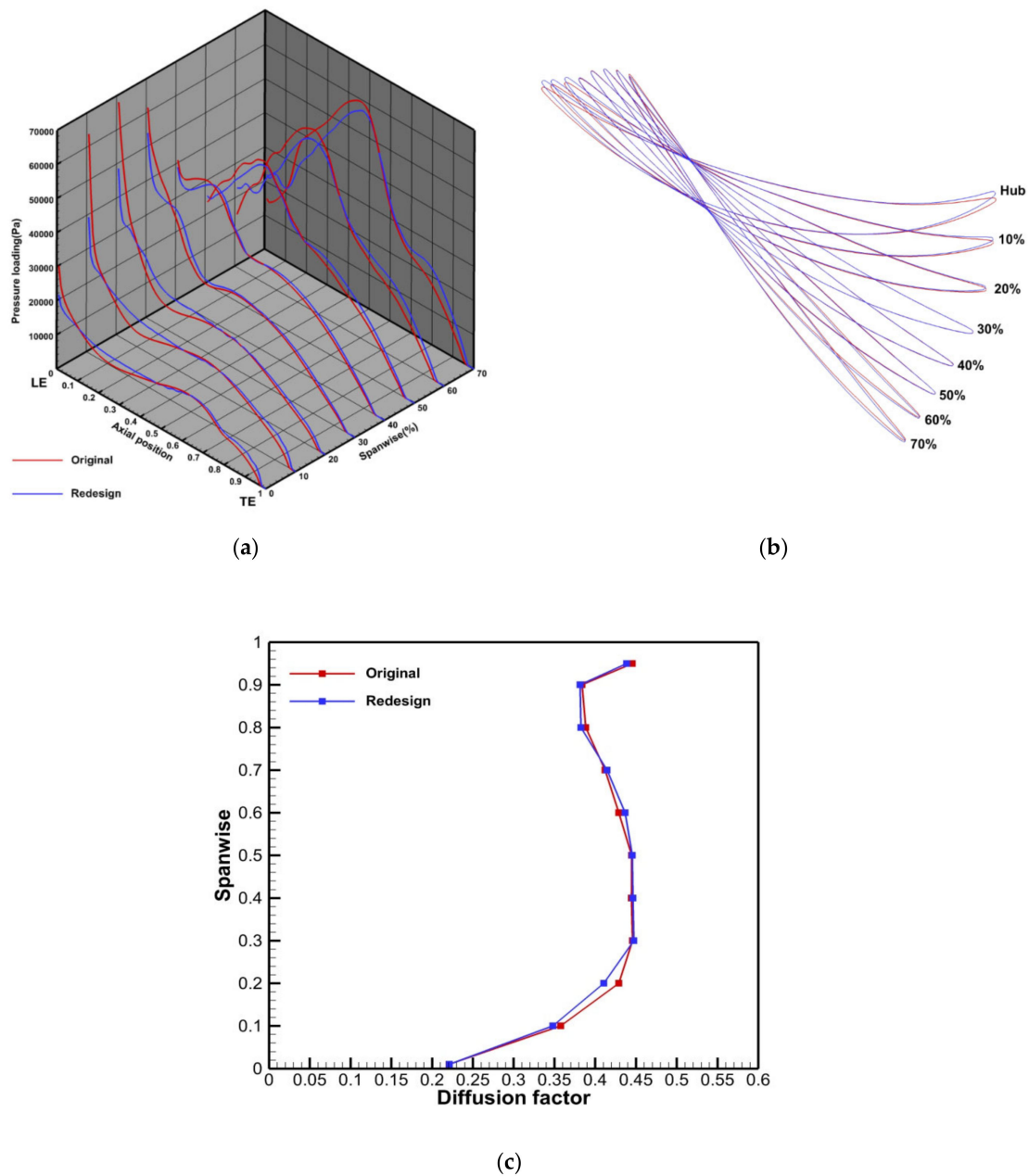


**Figure 14.** The pressure loading distributions, blade profiles, and diffusion factor distributions: (a) the pressure loading distributions on the original and redesigned blades, (b) the profiles of the original and redesigned blades, (c) the diffusion factor distributions along the spanwise direction.

The blue lines in Figure 14a plot the pressure loadings on the redesigned blade sections obtained from the inverse design. From the hub to the 40% span, it is found that the pressure loadings of the redesigned Rotor 67 at the leading edge are reduced. As a result, the attack angles are decreased when compared with the original Rotor 67 after the inverse design. Moreover, the pressure loading in the rear of the blade is released and spared some to the front of the blade. In this way, the pressure loading on the redesigned blade surfaces has a reasonable distribution. At the 50%, 60%, and 70% span, the peak pressure loading is reduced. This means that the strength of the shock wave is weakened. As a consequence, the total pressure loss caused by the shock wave is decreased. Furthermore, the risk of boundary layer separation induced from the shock-boundary layer interaction is also reduced due to the weakened shock. The blade profiles of the original and redesigned Rotor 67 at different spans are depicted, respectively, as red and blue lines in Figure 14b. It is observed that the metal angles of

leading edge are changed for decreased attack angles from the hub to the 40% span and the slopes on suction sides have delicate adjustments for the control of flow acceleration from the 50% to 70% span in the redesigned blade. The blade loading is assessed using the diffusion factor (DF) given by Lieblein et al. [26].

$$DF = 1 - V_2/V_1 + \Delta V_\theta/2\sigma V_1 \quad (13)$$

where  $V_1$  and  $V_2$  are the average velocities at the inlet and outlet of the blade rows.  $\Delta V_\theta$  is the change in tangent velocity when the flow pass through the blade rows.  $\sigma$  is the solidity. The diffusion factor distributions of original and redesigned rotors are compared and displayed in Figure 14c. It is showed that the diffusion factors of the redesigned rotor along the radial direction are almost unchanged compared with the original rotor.

The performance curves of original and redesigned blades are compared and depicted in Figure 15. It is indicated that the efficiencies are increased and the pressure ratios are almost unchanged at different mass flows. Furthermore, the efficiency of redesigned Rotor 67 is improved from 89.658% to 89.85% at the peak efficiency point with a slight increase in the pressure ratio and mass flow, as Table 1 shows.

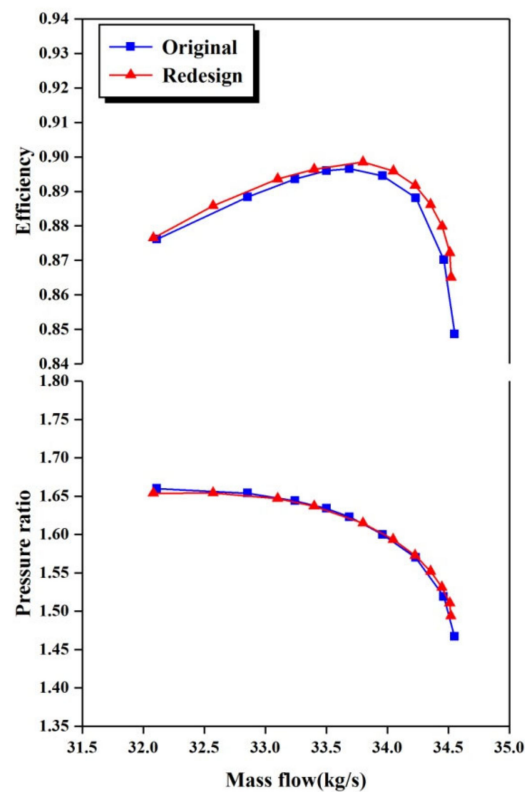


**Figure 15.** The performance curves of the original and redesigned Rotor 67.

**Table 1.** The performance of original and redesigned Rotor 67 at the peak efficiency point.

Rotor 67	Efficiency	Pressure Ratio	Mass Flow
Original	89.658%	1.61	33.69 kg/s
Redesign	89.85%	1.615	33.8 kg/s

#### 4.2. Stage 35 Redesign

The second case shows the redesign of transonic compressor Stage 35 using the inverse design system. This case demonstrates the potential application of inverse design in multi-row compressors. The essential parameters of Stage 35 are given in the open literature [27]. It can be seen from Figure 16 that the Stage 35 is a multi-row compressor which consists of a rotor and a stator. In the multi-row

environment, the flow interactions between the blade rows have strong impacts on the flow field. In this case, Stage 35 is used to explain how to improve the aerodynamic match between the blade rows and the resulting aerodynamic performance using the three-dimensional inverse design system.

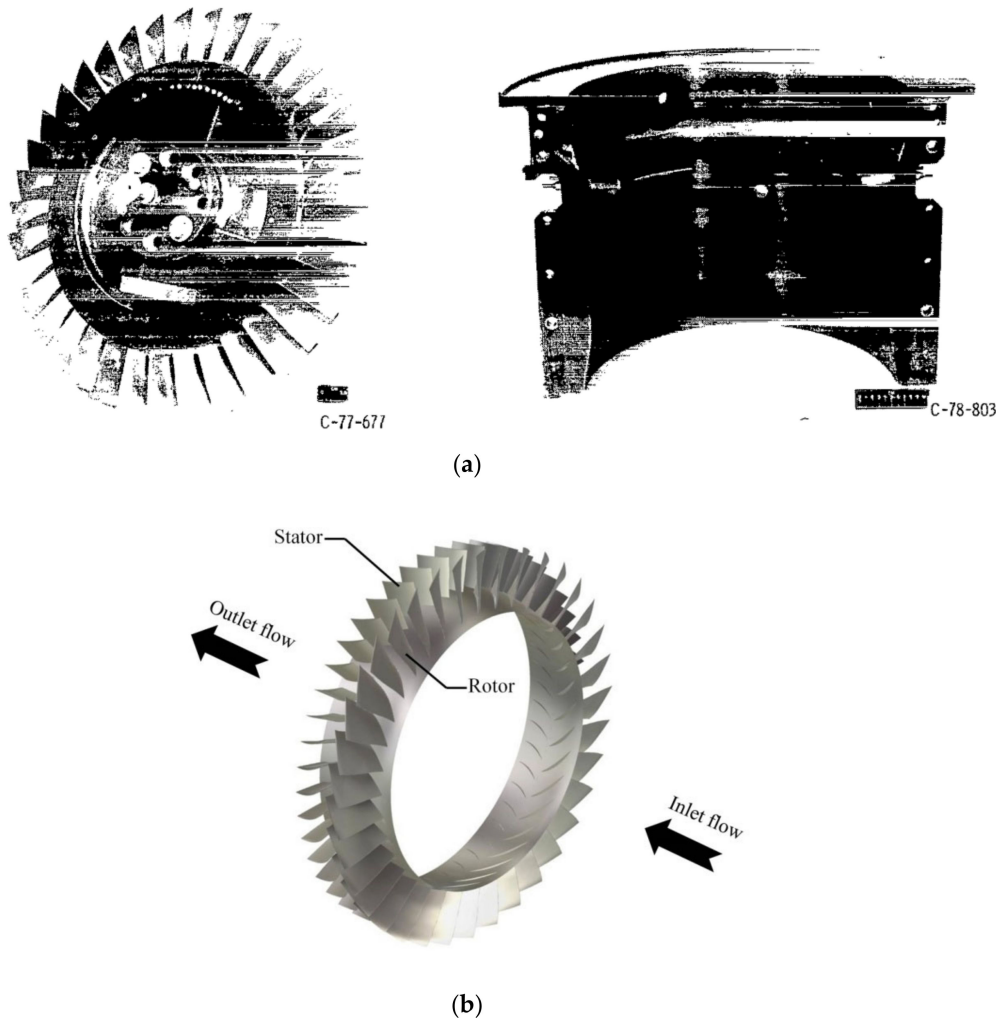


**Figure 16.** The physical model and the computational model of Stage 35: (a) the physical model, (b) the computational model.

The inverse design is implemented at the 10%, 20%, 30%, 40%, 50%, 60%, 70%, 80%, and 90% spanwise blade sections. The hub and tip blade sections are run in analysis mode and generated by linear extrapolation. At the peak efficiency point, the pressure loading distributions on the original stator blade are depicted in Figure 17a. It is found that the high-pressure loading resulted from an unreasonable aerodynamic match between the rotor and the stator locates near the leading edge region. This high loading would cause a decrease in the stage efficiency. Besides this, it will also increase the risk of flow separations and consequently induce the serious flow instability problem in the compressor. As a result, the original stator blade would be redesigned at the peak efficiency point to match the upstream flow, while the rotor blade is kept unchanged for the sake of simplification. The primary design target is to decrease the total pressure loss of the original stator and improve the stage efficiency by reorganizing the pressure loading distributions on the original stator blade.

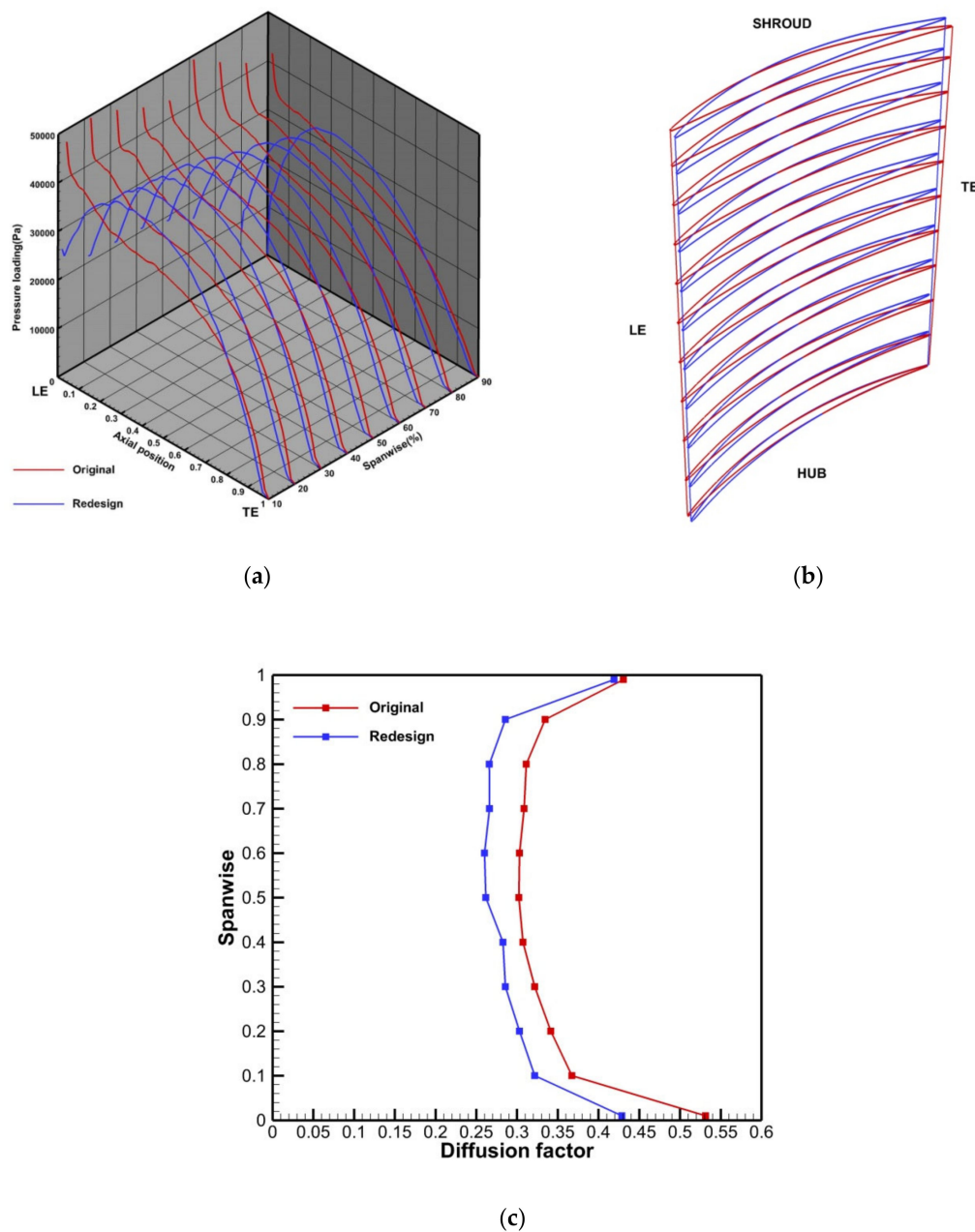


**Figure 17.** The pressure loading distributions, blade profiles, and diffusion factor distributions: (a) the pressure loading distributions of the original and redesigned Stage 35, (b) the blade profiles of the original and redesigned Stage 35, (c) the diffusion factor distributions along the spanwise direction.

The pressure loading distributions on the original and redesigned stator blades are compared in Figure 17a. It is observed that the pressure loading is decreased near the leading edge region in the redesigned stator. Furthermore, the peak loading in the redesigned stator increases to maintain the total pressure loading. The blade shapes of the original and redesigned stators are displayed in Figure 17b. The diffusion factor distributions of the original and redesigned blades are compared and displayed in Figure 17c. It is shown that the diffusion factors of the redesigned stator along the radial direction are generally decreased in contrast with the original blade. The changes in the diffusion factors are supposed to enhance the flow stability and the efficiencies of the redesigned Stage 35. This is confirmed by the characteristic lines of the original and the redesigned Stage 35, which are plotted in

Figure 18. It demonstrates that the efficiencies and the pressure ratios of the redesigned Stage 35 are generally improved near the stall boundary.

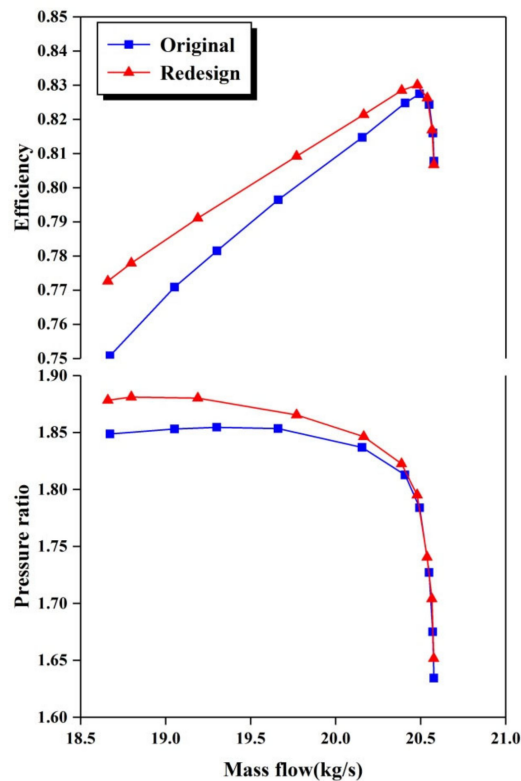


Figure 18. The performance curves of the original and redesigned Stage 35.

Table 2 shows the performance of the original and the redesigned Stage 35 at the peak efficiency point. It is shown that, due to the enhanced aerodynamic match of the redesigned Stage 35, the total pressure loss coefficient of the redesigned stator decreases from 0.046097 to 0.040918, and the peak stage efficiency of the redesigned Stage 35 increases from 82.749% to 83.011%. The performance curves of the original and the redesigned Stage 35 are depicted in Figure 18. It is indicated that the efficiencies and the pressure ratios of the redesigned Stage 35 are generally improved as they approach the stall boundary. It is also noted that there are few changes in the stall and choke mass flows.

Table 2. The performance of the original and the redesigned Stage 35 at the peak efficiency point.

Stage 35	Total Pressure Loss Coefficient (Stator)	Efficiency	Pressure Ratio	Mass Flow
Original	0.046097	82.749%	1.784	20.494 kg/s
Redesign	0.040918	83.011%	1.795	20.480 kg/s

## 5. Conclusions

In this paper, a three-dimensional inverse design system is implemented by linking the in-house inverse design module with the commercial CFD software NUMECA<sup>TM</sup>. This inverse design method respects wave-propagating characteristics on blade surfaces, which avoids the inconsistency caused by the enforcement of target pressure loading. The no-slip condition is also included to be consistent with the wall boundary condition used in the analysis solver. What is more, an improved blade update method and a modified relaxation factor are added to enhance the inverse design. The excellent reproduction of Rotor 67 in the recovery test shows the success of the inverse design system.

To explore the application of the developed inverse design system, two compressor redesign cases are implemented using the inverse design system. In the first case of redesigning the transonic fan Rotor 67, the pressure loading at the leading edge is reduced and the loading distribution is balanced on the blade surfaces located in the subsonic region. The peak loading is decreased on the blade sections located in the transonic region for weakening the shock wave. The redesigned Rotor 67 obtained from the inverse design system shows that the peak efficiency is improved from 89.658% to 89.85% with negligible changes in the pressure ratio and the mass flow. In the second case of redesigning the multi-row compressor Stage 35, the aerodynamic match in the redesigned Stage 35 is enhanced using the inverse design system to adjust the pressure loading on the stator located downstream. As a result, the total pressure loss coefficient of the redesigned stator decreases from 0.046097 to 0.040918 and the peak stage efficiency of the redesigned Stage 35 increases from 82.749% to 83.011%. Compared with the original Stage 35, the efficiencies and the pressure ratios of the redesigned Stage 35 are generally improved as they approach the stall boundary. However, there are few changes in the stall and choke mass flows.

**Author Contributions:** Y.D. constructed the inverse design system, implemented redesign cases, and wrote the paper. Q.Z. and B.J. helped to review and revise the manuscript. A.L. offered advice on post-processing and data visualization. W.Z. contributed with the usage of software. All authors have read and agreed to the published version of the manuscript.

**Funding:** This research was funded by National Science and Technology Major Project of China, grant number 2017-II-0006-0019.

**Conflicts of Interest:** The authors declare no conflict of interest.

## References

1. Lighthill, M. *A New Method of Two-Dimensional Aerodynamic Design*; Aeronautical Research Council R&M-2140; Aeronautical Research Council: London, UK, 1945.
2. Sanz, J.M. Automated Design of Controlled-Diffusion Blades. *J. Turbomach.* **1980**, *110*, 540–544. [[CrossRef](#)]
3. Lin, A.; Sun, Y.; Zhang, H.; Lin, X.; Yang, L.; Zheng, Q. Fluctuating characteristics of air-mist mixture flow with conjugate wall-film motion in a compressor of gas turbine. *Appl. Therm. Eng.* **2018**, *142*, 779–792. [[CrossRef](#)]
4. Lin, A.; Zheng, Q.; Jiang, Y.; Lin, X.; Zhang, H. Sensitivity of air/mist non-equilibrium phase transition cooling to transient characteristics in a compressor of gas turbine. *Int. J. Heat Mass Transf.* **2019**, *137*, 882–894. [[CrossRef](#)]
5. Dang, T.; Isgro, V. Euler-based inverse method for turbomachine blades, part 1: Two-dimensional cascades. *AIAA J.* **1995**, *33*, 2309–2315. [[CrossRef](#)]
6. Dang, T.; Damle, S.; Qiu, X. Euler-based inverse method for turbomachine blades, part 2: Three-dimensional flows. *AIAA J.* **2000**, *38*, 2007–2013. [[CrossRef](#)]
7. Tiow, W.T.; Zangeneh, M. Application of a three-dimensional viscous transonic inverse method to nasa rotor 67. *Proc. Inst. Mech. Eng. Part A J. Power Energy* **2002**, *216*, 243–255. [[CrossRef](#)]
8. Qiu, X. A Fully Three-Dimensional Inverse Method for Turbomachine Blade Aerodynamic Design. Ph.D. Thesis, Syracuse University, Syracuse, NY, USA, 1999.
9. Demeulenaere, A.; Van den Braembussche, R. Three-Dimensional Inverse Method for Turbomachinery Blading Design. *J. Turbomach.* **1998**, *120*, 247–255. [[CrossRef](#)]
10. Zangeneh, M.; Goto, A.; Harada, H. On the Design Criteria for Suppression of Secondary Flows in Centrifugal and Mixed Flow Impellers. *J. Turbomach.* **1998**, *120*, 723–735. [[CrossRef](#)]
11. Watanabe, H.; Zangeneh, M. Design of the Blade Geometry of Swept Transonic Fans by 3D Inverse Design. In Proceedings of the ASME Turbo Expo 2003, Atlanta, GA, USA, 16–19 June 2003; pp. 603–612. [[CrossRef](#)]
12. Bonaiuti, D.; Zangeneh, M. On the Coupling of Inverse Design and Optimization Techniques for the Multiobjective, Multipoint Design of Turbomachinery Blades. *J. Turbomach.* **2009**, *131*, 021014. [[CrossRef](#)]
13. Van Rooij, M.P.C.; Dang, T.Q.; Larosiliere, L.M. Improving Aerodynamic Matching of Axial Compressor Blading Using a Three-Dimensional Multistage Inverse Design Method. *J. Turbomach.* **2007**, *129*, 108–118. [[CrossRef](#)]



14. Daneshkhah, K.; Ghaly, W. Aerodynamic Inverse Design for Viscous Flow in Turbomachinery Blading. *J. Propuls. Power* **2007**, *23*, 814–820. [[CrossRef](#)]
15. Thompkins, W.T.; Tong, S.S. Inverse or Design Calculations for Non-Potential Flow in Turbomachinery Blade Passages. In Proceedings of the ASME 1981 International Gas Turbine Conference and Products Show, Houston, TX, USA, 9–12 March 1981. [[CrossRef](#)]
16. Tong, S.S.; Thompkins, W.T. A Design Calculation Procedure for Shock-Free or Strong Passage Shock Turbomachinery Cascades. *J. Eng. Gas Turb. Power* **1983**, *105*, 369–376. [[CrossRef](#)]
17. Van Rooij, M.P.C.; Medd, A. Reformulation of a Three-Dimensional Inverse Design Method for Application in a High-Fidelity CFD Environment. In Proceedings of the ASME Turbo Expo 2012: Turbine Technical Conference and Exposition, Copenhagen, Denmark, 11–15 June 2012; pp. 2395–2403. [[CrossRef](#)]
18. Mileshin, V.I.; Orekhov, I.K.; Shchipin, S.K.; Startsev, A.N. New 3D Inverse Navier-Stokes Based Method Used to Design Turbomachinery Blade Rows. In Proceedings of the ASME 2004 Heat Transfer/Fluids Engineering Summer Conference, Charlotte, NC, USA, 11–15 July 2004; pp. 881–889. [[CrossRef](#)]
19. Shumal, M.; Nili-Ahmadabadi, M.; Shirani, E. Development of the ball-spine inverse design algorithm to swirling viscous flow for performance improvement of an axisymmetric bend duct. *Aerosp. Sci. Technol.* **2016**, *52*, 182–188. [[CrossRef](#)]
20. Yang, J.; Liu, Y.; Wang, X.; Wu, H. An improved steady inverse method for turbomachinery aerodynamic design. *Inverse Probl. Sci. Eng.* **2017**, *25*, 633–651. [[CrossRef](#)]
21. Strazisar, A.; Wood, J.; Hathaway, M.; Suder, K. *Laser Anemometer Measurements in a Transonic Axial-Flow Fan Rotor*; NASA Technical Report; NASA: Washington, DC, USA, 1989; Volume 90, pp. 430–437.
22. Zheng, R.; Xiang, J.; Sun, J. Blade Geometry Optimization for Axial Flow Compressor. In Proceedings of the ASME Turbo Expo 2010: Power for Land, Sea, and Air, Glasgow, UK, 14–18 June 2010; pp. 633–644. [[CrossRef](#)]
23. Kuang, H.; Chu, W.; Zhang, H.; Ma, S. Flow mechanism for stall margin improve-ment via axial slot casing treatment on a transonic axial compressor. *J. Appl. Fluid Mech.* **2017**, *10*, 703–712. [[CrossRef](#)]
24. Zhou, X.; Zhao, Q.; Cui, W.; Xu, J. Investigation on axial effect of slot casing treatment in a transonic compressor. *Appl. Therm. Eng.* **2017**, *126*, 53–69. [[CrossRef](#)]
25. Zhang, H.; Liu, W.; Wang, E.; Chu, W.; Ding, K.; Yan, S. Effect of inverse blade angle slots on a transonic rotor performance and stability. *Aerosp. Sci. Technol.* **2020**, *96*, 105596. [[CrossRef](#)]
26. Lieblein, S.; Schwenk, F.C.; Broderick, R.L. *Diffusion Factor for Estimating Losses and Limiting Blade Loadings in Axial-Flow-Compressor Blade Elements*; NASA Technical Report; NASA: Washington, DC, USA, 1953.
27. Reid, L.; Moore, R.D. *Performance of Single-Stage Axial-Flow Transonic Compressor with Rotor and Stator Aspect Ratios of 1.19 and 1.26, Respectively, and with Design Pressure Ratio of 1.82*; NASA Technical Paper 1338; NASA: Washington, DC, USA, 1978.

**Publisher’s Note:** MDPI stays neutral with regard to jurisdictional claims in published maps and institutional affiliations.



© 2020 by the authors. Licensee MDPI, Basel, Switzerland. This article is an open access article distributed under the terms and conditions of the Creative Commons Attribution (CC BY) license (<http://creativecommons.org/licenses/by/4.0/>).